# Laboratory Investigation of Beach Scarp and Dune Recession Due to Notching and Subsequent Failure

Erikson, Li; Larson, Magnus; Hanson, Hans

*Published in:*
Marine Geology

*DOI:*
10.1016/j.margeo.2007.04.006

2007

ELSEVIER

Marine Geology 245 (2007) 1 – 19

MARINE GEOLOGY
INTERNATIONAL JOURNAL OF MARINE GEOLOGY, GEOCHEMISTRY AND GEOPHYSICS

www.elsevier.com/locate/margeo

# Laboratory investigation of beach scarp and dune recession due to notching and subsequent failure

Li H. Erikson *, Magnus Larson, Hans Hanson

*Department of Water Resources Engineering, Lund University, Box 118, 221 00, Lund, Sweden*

Received 9 May 2006; received in revised form 31 March 2007; accepted 9 April 2007

**Abstract**

Analytical models to calculate notch development and subsequent mass failure of dunes are presented. The notch evolution model is based on a transport equation for sediment from the dune and the sediment volume conservation equation, whereas the models of mass failure are derived using elementary engineering statics and soil mechanics. An empirical transport coefficient in the model describing the notch growth rate is found to be related to the hydrodynamic forcing at the dune normalized by geotechnical parameters describing the resistive strength of the dune. Two modes of mass failure are modeled whereby the overhang generated by the removal of material from the dune foot (notching) slides downward or topples over following the development of a tensile crack some distance shoreward of the maximum notch depth. The accuracy of the notch evolution and mass failure models are assessed by comparing calculated recession distances against measurements from a small-scale laboratory experiment.


*Keywords:* dunes; beach scarps; tensile strength; notching; wave impact

## 1. Introduction

The aim of this study was to investigate erosion mechanisms of beach sand formations such as scarps and dunes undergoing wave attack. Although the physical scale of scarps and dunes can differ by an order of magnitude, the mechanisms are often similar. Recession typically occurs as a result of a series of steps (Carter et al., 1990). As waves begin to attack a scarp or dune, erosion causes an increased face steepness. Continued wave attack is focused at the foot of the formation and typically causes undercutting or removal of the scarp or dune foot (notching). The undercutting leads to a state of tension in the upper part with visible tension cracks parallel to the face. This can readily be observed in beach scarps undergoing attack by swash waves, but is also a common mechanism of dune recession as pointed out by Carter and Stone (1989). The resulting overhang generated by the tensile crack alters the balance of forces and eventually succumbs to a mass failure whereby a slab of sand slides downward or topples over leaving a vertical face. The sediment from the mass failure lands at the foot of the scarp or dune and provides temporary protection. If wave attack continues, the failed slab material is removed by wave action and further undercutting occurs followed by mass failure, continuing the cycle.

Because dunes are of greater importance than beach scarps, much experimental and theoretical work has

* Corresponding author. 2601 Hambleton Lane, Santa Cruz, CA 95065, USA. Tel.: +1 831 476 8582.
*E-mail address:* Li.Erikson@sbcglobal.net (L.H. Erikson).

0025-3227/$ - see front matter © 2007 Elsevier B.V. All rights reserved.
doi:10.1016/j.margeo.2007.04.006

focused on dune, as opposed to scarp, recession. Most predictive models of dune recession focus on storm surges in conjunction with assumed post-storm profiles. An alternative approach, whereby no post-storm profile is assumed, but where erosion from the impact of individual waves is used to determine the amount eroded, was proposed by Fisher and Overton (1984) and Nishi and Kraus (1996). The frequency and intensity of wave impacts, multiplied by an empirical transport coefficient, determine the total amount eroded. Wave impact theory has been empirically validated and successfully employed to simulate dune erosion in small and large wave tank studies and in the field (Fisher and Overton, 1984; Fisher et al., 1986; Overton and Fisher, 1988; Overton et al., 1994; Nishi and Kraus, 1996); however, little has been done in developing a predictive equation for the transport coefficient. Furthermore, the modeling has focused on describing the gross features of dune erosion and no attempt has been made to resolve the details of the process.

A small-scale wave tank experiment was conducted in this study to obtain a better understanding of the short-term time-evolution of dunes during erosion by individual waves. The experimental data should be directly applicable to scarps at natural scale, and assuming that the scaling model described later is valid, the results should also hold for small dunes. Recession of the experimental dunes was observed to occur as the result of a two-step process described by notching and slumping or notching and toppling, similar to the description of dune recession presented by Carter et al. (1990). In this paper, a distinction is made between dune erosion and recession, such that erosion refers to removal of material from the lower part of the dune (notching), and recession refers to the landward movement of the entire dune face (mass wasting). Two modes of mass wasting were observed and are described as shear- and beam-type failures (Fig. 1). Shear failure is hypothesized to occur when the weight of the overhang (resulting from notching) exceeds the shear strength of the sediment and it slides downward as depicted in Fig. 1a–b. Beam-type failures occur when tension cracks develop some distance landward of the dune face and the pending failure block either rotates or slides downward (Fig. 1c–d).

Development of the governing equations and associated analytical solutions are described in the following section. The first equation estimates the rate of sediment removal (erosion) from the dune foot by undercutting or notching, allowing for a description of the temporal growth of the notch. Laboratory observations regarding the shape of the notch at the dune foot were incorporated into the model and, thus, may only be representative

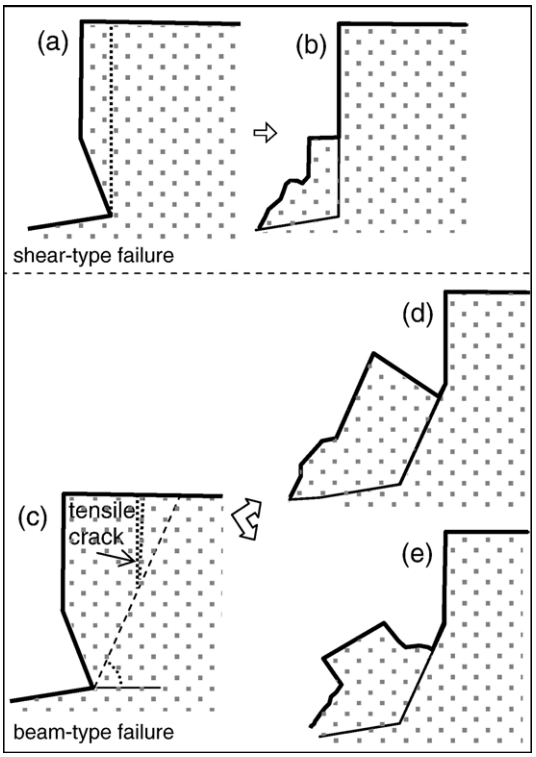


Fig. 1. Conceptual sketch of shear- and beam-type failure mechanisms.

of toe erosion from the impact of fully broken bores. The second set of equations estimates the maximum recession distance based on two different observed mass failure modes. The model shows that the recession distance and time at which failure occurs is related to the notch depth. Following a description of the laboratory experiment, a summary of the experimental data is presented after which model calibration and validation are discussed.

## 2. Theoretical development

### 2.1. Dune toe erosion by notching

#### 2.1.1. Governing equations

Assuming that the geometry of the notch can be specified at any instant in time, notch progression can be calculated if the volume eroded due to the impact of waves can be predicted. Fisher and Overton (1984) proposed a model for dune erosion where the impact force of individual waves is linearly related to the volume of sand eroded or, as presented by Nishi and Kraus (1996), linearly related to the weight of eroded sand,

$$\Delta W = C_E F \tag{1}$$

where $C_E$ is an empirical coefficient, $F$ the force exerted by the impact of waves on the dune, and $\Delta W = \Delta V \rho_s (1-p)g$, the weight of the eroded volume $\Delta V$, $\rho_s$, the specific soil density, $p$ porosity, and $g$ the acceleration due to gravity. The impacting force is derived by considering a bore propagating upslope and changing its rate of momentum as it impacts the dune face (Cross, 1967),

$$F_o = \rho u_{inc}^2 h_{inc} \tag{2}$$

where $\rho$ is the water density, $u_{inc}$ the incident bore speed, and $h_{inc}$ the bore height. The incident bore speed in Eq. (2) can be estimated with (Cross, 1967; Miller, 1968),

$$u_{inc} = C_u \sqrt{g h_{inc}} \tag{3}$$

where $C_u$ is an empirical coefficient between 1 and 2 related to the frictional resistance. Combining Eq. (2) with Eq. (3) and adding the term $\Delta t/T$ to represent the number of bores with wave period $T$ impacting the dune during a given time, $\Delta t$, yields a total swash force proportional to $u_{inc}^4$:

$$F = \rho(u_{inc}^4/(gC_u^2))(\Delta t/T). \tag{4}$$

Combining Eqs. (1) and (4) and doing some rearranging, and letting $\Delta t$ approach zero, gives the rate of erosion in terms of the incident bore velocity,

$$\frac{dV_E}{dt} = \frac{C_E}{C_u^2}\frac{1}{1-p}\frac{\rho}{\rho_s}\frac{u_{inc}^4}{g^2 T} = \frac{K_d}{1-p}\frac{\rho}{\rho_s}\frac{u_{inc}^4}{g^2 T} \tag{5}$$

where $V_E$ is the eroded volume and $K_d$ was introduced to replace the empirical relationship, $C_E/C_u^2$.

In order to analytically predict the notch depth with Eq. (5), a description of notch geometry is necessary. Cross-section profiles and evolution of the notches in the laboratory experiments are shown in Fig. 2. The profile following the impact of every other bore is shown in Fig. 2a whereas the profile following every other wave train is shown in Fig. 2b. A summary of the experimental cases, including wave conditions, is further discussed in Section 3. The profile plots are discussed and presented here to clarify the assumptions made regarding the notch shape.

The plots in Fig. 2 show that the slopes along the bottom of the notch and in front of the dune are approximately constant and more or less parallel to the initial foreshore slope (tan $\beta$). This similarity in slope suggests that the transport mechanisms controlling the bottom profile are the same in these two regions, that is, shear-stress-related transport. Schematically, the upper portion of the notch may be described by a linear or a power function, so that following the impact of each bore (Fig. 2a) or set of waves (Fig. 2b), the entire notch maintains a triangular shape, or an upper part that is either convex or concave. Referring to the definition sketch in Fig. 3 and assuming a power- or triangular-shaped notch, the geometry is given by,

$$\begin{aligned} x(z) &= b_1(z/B)^m \quad 0 \le z \le B \\ x(z) &= b_1(-z/(a-B))\ 0 \ge z \ge B-a \end{aligned} \tag{6}$$

where $a$ is the height of the notch at the dune face, $b_1$ the maximum width of the notch, $B$ the notch height measured from the elevation of the maximum notch depth, $m$ an exponent describing the shape of the upper part of the notch ($m<1$ gives a convex shape whereas $m>1$ gives a concave shape), and $x$ and $z$ are coordinates with their origin at the maximum notch depth, located at elevation $z_o$. Note that for $m=1$, the upper part of the notch is linear so that the notch shape is triangular. In this schematization, notch evolution will always progress so that the lower part of the notch has a slope in agreement with the foreshore slope. In a predictive mode, $a$ is specified from the wave properties and $b_1$ is the unknown variable employed to describe the notch evolution.

### 2.1.2. Notch evolution

The volume per unit length in the transverse direction of a triangular-shaped notch is,

$$V_E = 0.5ab_1 = 0.5C_a(R-z_{in})((z_o-z_{in})/\tan\beta) \tag{7}$$

where $R$, $z_o$, and $z_{in}$ are referenced from the still water line (SWL) or still-water shoreline (SWS), $z_o$ is the height of the most landward point of the notch, $z_{in}$ the foreshore elevation corresponding to the dune face, and $b_1 = (z_o - z_{in}/\tan\beta)$ from geometry. It was assumed that the top of the notch corresponds to the runup limit including additional height from the reflected bore impacting the dune face such that $a = C_a(R-z_{in})$, where $R-z_{in}$ is the estimated incident bore height, and $C_a$ is an empirical constant greater than one introduced to account for the increased contact area between the bore and dune face (the validity of this assumption is discussed in the results section). The more general case of a power-shaped notch is not discussed here, although an analytical solution for this case has also been derived.

The rate of change of $V_E$ can be expressed as:

$$\frac{dV_E}{dt} = \frac{dV_E}{dz_o}\frac{dz_o}{dt} = \frac{1}{2}\frac{C_a(R-z_{in})}{\tan\beta_{fs}}\frac{dz_o}{dt}. \tag{8}$$

Combining Eqs. (5) and (8), along with an estimate of the bore velocity at the dune face based on ballistics theory $u_{inc}^2 = u_s^2 - 2gz_o$ ($u_s$=bore velocity at the SWS), and a first-order estimate of the maximum runup height excluding friction (Shen and Meyer, 1963), $R = u_s^2/2g$, yields a governing equation describing the evolution of $z_o$:

$$\frac{dz_o}{dt} = \frac{8K_d}{1-p}\frac{\rho}{\rho_s}\frac{\tan\beta_f}{C_a(R-z_{in})}\frac{(R-z_o)^2}{T}. \quad (9)$$

This equation is separable and may be solved employing the initial condition that $z_o = z_{in}$ at time $t=0$. With some rearranging and noting the geometric relationship between $b_1$ and $z_o$, previously discussed, the growth of the maximum notch width, assuming that $C_e\, t/T$ is small, may be expressed as a linear growth with time such that,

$$b_1 = \lfloor (C_a(R-z_{in}))/\tan\beta_f \rfloor \cdot [C_e t/T] \quad (10)$$

where

$$C_e = [(8K_d)/(1-p)] \cdot [\rho/\rho_s] \cdot \tan\beta_f. \quad (11)$$

### 2.2. Mass failure

#### 2.2.1. Shear-type mass failure

Shear failure occurs when the weight of the overhang (resulting from notching) exceeds the shear strength of the sediment and it slides downward as schematized in Fig. 1a–b. A definition sketch is shown in Fig. 4a, where the shaded part of the dune represents the pending failure slab. Assuming a triangular-shaped notch the critical case is examined so that the forces are balanced and the block is in a state of static equilibrium immediately before failure (Thorne and Tovey, 1981). The forces are resolved vertically, and assuming a unit width, the weight, $W_s$, of the failure slab at failure is,

$$W_s = \gamma b_{2shr}(A - B/2) \quad (12)$$

where $\gamma$ is the weight of soil at natural moisture content, $b_{2shr}$ is the width of the failure slab equal to the critical notch depth, $b_{1cr}$, and, assuming no accumulation of sand on the foreshore, $A = D_o - b_1 \tan\beta$, where $D_o$ is the initial dune height, and $B = A - D_s$ or $B = a - b_1 \tan\beta$.

The force $F_s$ generated by the shear stress that balances $W$ just before collapse is given by,

$$F_s = \tau_{cr}(D_s + B/3) \quad (13)$$

where $\tau_{cr}$ is the critical shear stress when mass failure occurs, and $D_s + B/3$ is the length over which the shear strength, maintaining the overhang, acts. The last term, $B/3$, reflects the assumption that the shear stress of the triangular-shaped part of the overhang acts along the length from the top of the said shape to its center of gravity. If the critical shear stress is assumed to equal the shear strength of the soil at failure, the overhang is expected to fall when its weight exceeds the shear strength of the soil, so that from Eqs. (12) and (13):

$$b_{2shr} \geq (\tau_{cr}(D_s + B/3))/\gamma(A - B/2). \quad (14)$$

The shear strength at failure in a non-cohesive soil can be described by the revised Coloumb equation (Öberg, 1997),

$$\tau_{cr} = \sigma_n \tan\phi' + S(u_a - u_w)\tan\phi' \quad (15)$$

where $\sigma_n$ is the normal stress on the failure plane, $\phi'$ the internal friction angle, $(u_a - u_w)$ the soil suction, and $S$ the saturation level ($0<S<1$). On a vertical failure plane, the normal stress ($\sigma_n$) is zero leaving a shear strength that is only a function of the matrix suction, saturation level, and internal friction angle. Soil suction is often ignored in many engineering slope stability analyses and instead accounted for by using a fictitious cohesion. In this study, soil suction is explicitly accounted for and it is this parameter that enables eroding dunes to exhibit the frequently observed vertical fronts (Carter et al., 1990).

Soil suction consists of two components: matrix and osmotic suction. Matrix suction is a function of the pore volume between sediment grains and amount of water contained in the soil matrix. In the case of a wetted dune, the pores are occupied by both water and air. At the interface between air and water, the difference between the inward attraction results in an interfacial tension which provides strength and stability to the dune. The strength and stability increases with increasing water content (by weight) up to about 10 to 15%, and decreases as increased water content reduces, and ultimately eliminates, the surface tension effect of the pore water. Osmotic suction is related to the presence of chemicals, such as salt, in the pore water, which should be accounted for in the case of dunes in contact with saltwater. In this study, models were developed and tested against laboratory studies with freshwater so that osmotic suction was not likely present and not accounted for. Soil suction and matrix suction are used interchangeably throughout this paper.

*2.2.2. Beam-type mass failure or failure by tensile cracking*

The second mode of mass failure observed in the laboratory experiments was beam failure. This type of failure appears to occur by initial tensile cracking at the top of the dune, followed by either shear failure along an internal failure plane or overturning of the pending failure block due to the moment generated by the overhang (Fig. 1c–e).

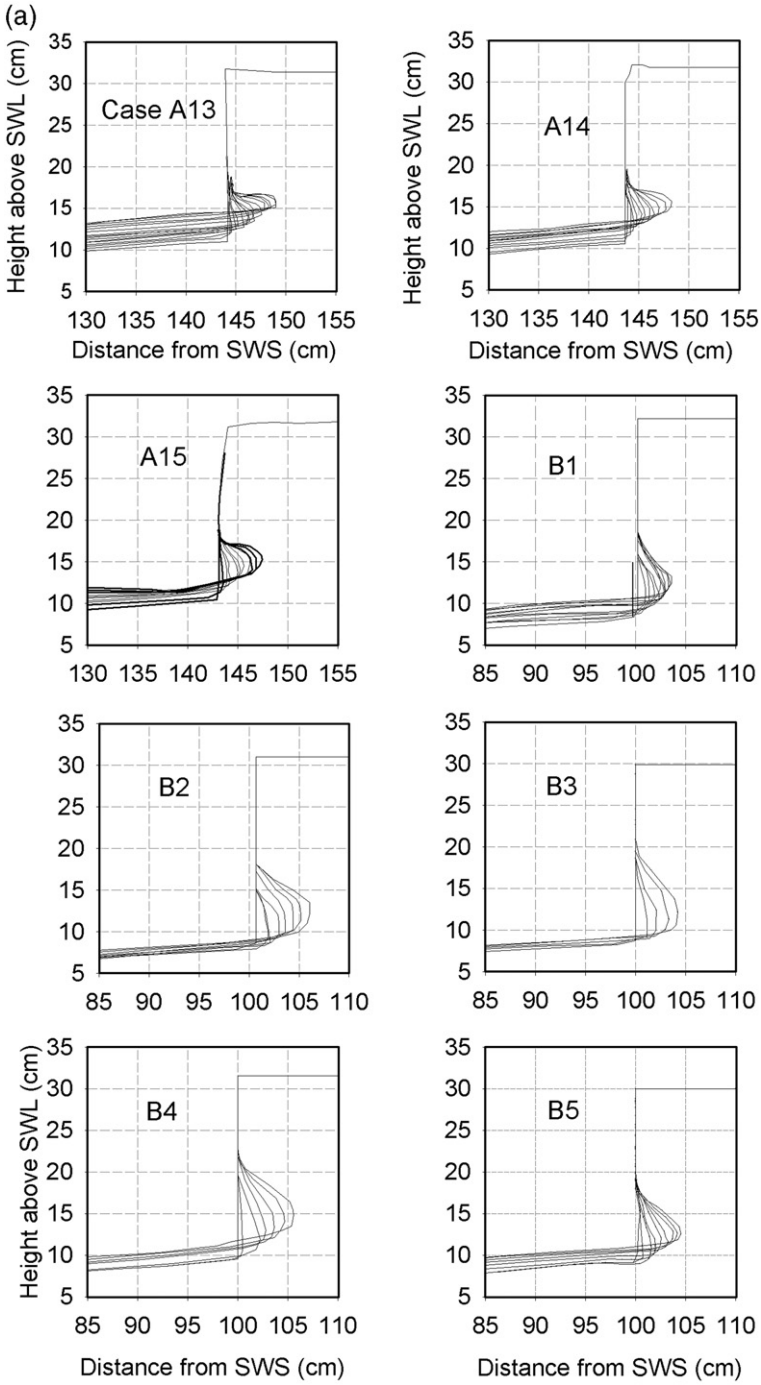


Fig. 2. a. Notch development of experimental dunes subjected to fully broken solitary waves. Profiles following the impact of every other bore are shown. b. Notch development of the experimental dunes subjected to impacting wave groups. Profiles following every wave packet are shown.

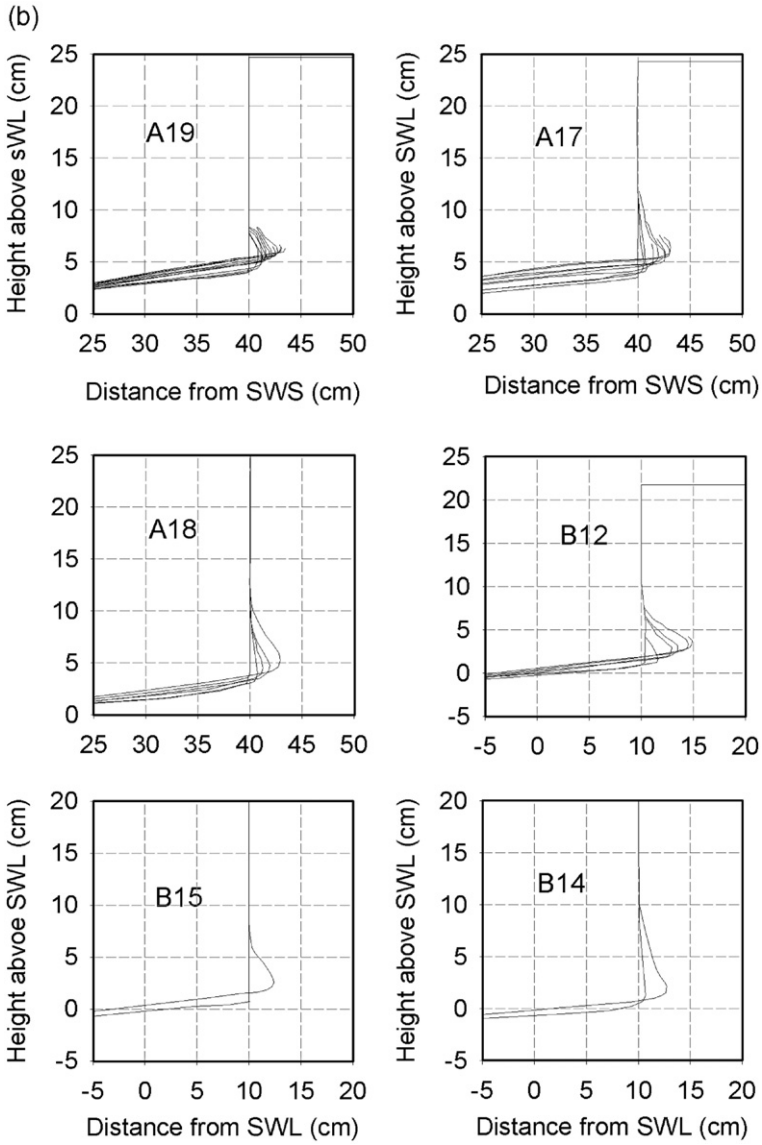


Fig. 2 (*continued*).

It is hypothesized that tensile failure (vertical tension crack that forms some distance back from the dune face and landward of the notch depth, $b_1$) occurs due to lateral earth pressures and the weight of the overhang. The overhang causes a moment and a bending stress at the top of the dune (with the bending stress being analogous to that generated by a cantilever beam). When the total stress exceeds the tensile strength of the soil, cracking begins and migrates downward until it intersects with an internal failure plane (Fig. 1c) that is typically considered to be at the angle $\alpha \approx 45° + \phi'/2$ from the horizontal in non-cohesive soils (Terzaghi and Peck, 1948). Here, failure continues if the force generated by the gliding weight of the failing slab exceeds the shear strength of the soil, $\tau_{cr}$ along the failure plane so that the failing block slides downward and lands with the top surface pointing upward as depicted in Fig. 1d. If the shear strength is sufficient to keep the pending failure block from sliding downward, failure might still occur if the overturning moment of the failing block exceeds the resisting moment and the block topples over as depicted in Fig. 1e.

Tensile cracking is well recognized in the field of slope stability analysis. Lohnes and Handy (1968) applied

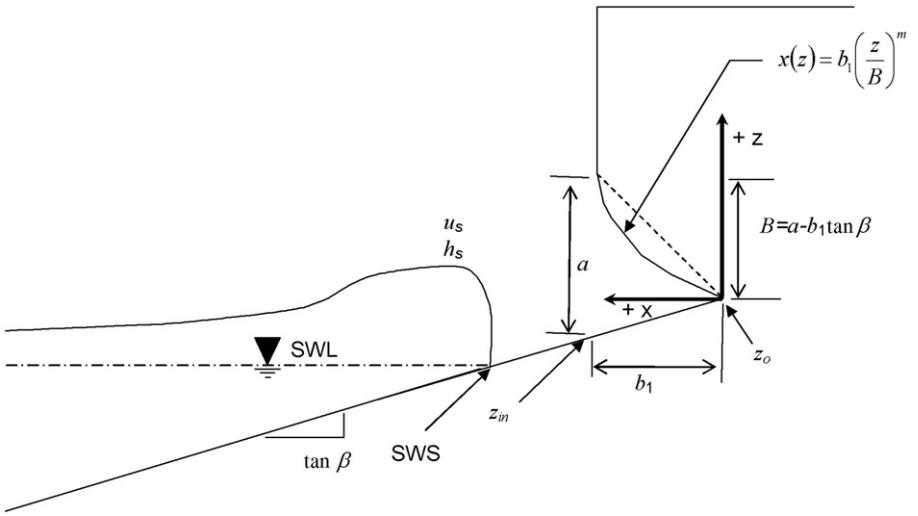


Fig. 3. Definition sketch of dune erosion by notching.

Rankine–Bell earth-pressure theory along with equations developed by Terzaghi (1943) and presented a model to predict the recession distance of steep cohesive slopes without notching. Clean sands however, are cohesionless and as such a new approach based on the method presented by Lohnes and Handy (1968) was developed to predict failure of non-cohesive steep slopes affected by notching.

The geometric shape of a pending failure block is shown in Fig. 4b along with required dimensions. The slope of the internal failure plane is estimated to be at $\alpha$ from the horizontal ($\alpha_c=45°-\phi'/2$ from the vertical) and is assumed to start at the maximum notch depth. In the figure, it can be seen that the recession distance due to beam failure, $b_{2beam}$, can be found from geometry,

$$b_{2beam} = b_1 + b_3 \tag{16}$$

where $b_3=(A-Z_c)$ tan $\alpha_c$ and $Z_c$=depth of the tensile crack. The notch depth, $b_1$, can be found with Eq. (10) and assuming no foreshore accumulation, $A=D_o-b_1$ tan $\beta$. Predicting the recession distance due to beam failure using Eq. (16), then reduces to finding a tensile crack, $Z_c$, long enough to intersect with the internal failure plane.

The depth of tensile cracking is estimated by assuming that the tensile stress decreases linearly with depth from the top surface and that the total tensile stress exceeds the soil tensile strength so that,

$$Z_c = Z_t(1-(\sigma_t/\sigma_{ss})) \qquad \text{for } \sigma_{ss}>\sigma_t \tag{17}$$

where $\sigma_t$ is the soil tensile strength, $\sigma_{ss}$ the tensile stress at the surface, and $Z_t$ the depth of soil tension.

*2.2.3. Tensile strength*

The tensile strength of the soil is assumed to be uniform throughout the dune. Several theoretical and experimental studies have shown that soil tensile strength is closely related to water content and that it increases non-linearly with increasing matrix suction (e.g., Kim and Hwang, 2003). The equations used to calculate tensile strength for this study are based on the approach presented by Pierrat and Caram (1997) and relations developed by Schubert (1972) so that,

$$\begin{aligned}\sigma_t &= \sigma_{pz}((S_c-S)/(S_c-S_f)) \\ &\quad +\sigma_{cz}((S-S_f)/(S_c-S_f)) \\ &\text{where } \sigma_{pz} = 0.26[(1-e)/(eD_{50})] \\ &\text{and } \sigma_{cz} = S[7(((1-e)/e)(0.0727/D_{50}))]\end{aligned} \tag{18}$$

and $e$ is the porosity, $D_{50}$ the median grain size diameter, $S$ the *in situ* saturation level, $S_c$ (=90%) the upper saturation limit for the "funicular state", and $S_f$ the upper saturation limit for the pendular state when liquid bridges form (34%, Flemmer, 1991).

*2.2.4. Tensile stress and depth of tension due to lateral earth pressures*

The tensile stress at the top surface, $\sigma_{ss}$, is estimated to be the sum of the lateral earth pressure and the bending stress caused by the overhang

$$\sigma_{ss} = |\sigma_{LEPs} + \sigma_{bs}| \tag{19}$$

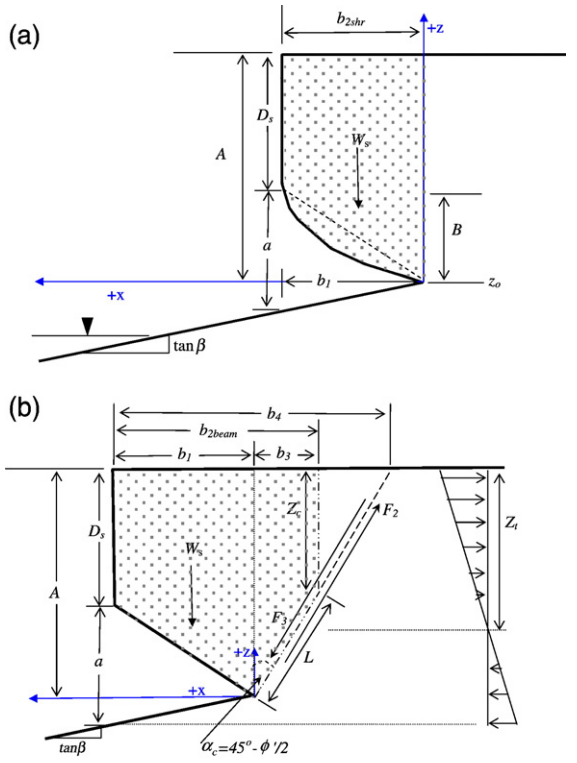


Fig. 4. Definition sketch of (a) shear-type and (b) beam-type mass failure.

where $\sigma_{LEPs}$ is the tensile stress due to lateral earth pressure at the surface, and $\sigma_{bs}$ the bending stress at the surface.

In a non-cohesive, unsaturated soil matrix, with or without an unbraced cut but without an overhang, the stress due to lateral earth pressures at any depth, $d$, is (Lu and Likos, 2004),

$$\sigma_{LEP} = (\gamma d)K_u - S(u_a - u_w)(1 - K_u) \quad (20)$$

where $K_u$ is a coefficient of earth pressure, and the first term on the right-hand-side is the compressive pressure due to the self weight of the overlying material (using Rankine earth pressure theory), and the second term represents tension caused by matrix suction. Assuming that the suction stress is constant with depth and the soil is homogeneous, a conceptual diagram of the two components is shown in Fig. 5.

The Rankine earth pressure (shown as a stress increasing linearly with depth) is similar to fluids in that the vertical pressure due to a soil layer of depth $d$ can be estimated with $\gamma d$. Unlike fluids, however, soil can support shear loads, and thus, the horizontal pressure is not the same as the vertical pressure. A coefficient of earth pressure, $K_u$, dependent on the angle of internal friction $\phi'$ where $K_u = \tan^2(45° - \phi'/2)$, is used to calculate the horizontal pressure from the vertical pressure. The coefficient of earth pressure is used in the calculation of the tensile stress due to matrix suction as well as in Eq. (20).

The combined effect of the Rankine earth pressure and suction stress, shown in Fig. 5, results in a linear lateral-earth-pressure profile with the upper portion in tension and the lower in compression. It is within the zone of tension that tensile cracking is expected. The depth of the tension zone can be found by normalizing Eq. (23) with the vertical stress. Assuming that the vertical stress at depth $d$ can be represented by $\gamma d$, a coefficient of active earth pressure for unsaturated soil, $K_{au}$, can be defined (Lu and Likos, 2004),

$$K_{au} = \sigma_{LEP}/\gamma d = K_u - [(S(u_a - u_w))/\gamma d] \cdot [1 - K_u]. \quad (21)$$

The resulting earth pressure profile changes from tension to compression when $K_{au}$ is zero and $d = Z_t$ so that from Eq. (25),

$$Z_t = [(S(u_a - u_w))/\gamma] \cdot [1/K_a - 1]. \quad (22)$$

It is also clear from Fig. 5 and Eq. (23) that the lateral earth pressure at the surface ($d=0$) is solely due to the matrix suction so that the tensile stress due to the lateral earth pressure at the surface is,

$$\sigma_{LEPs} = -S(u_a - u_w)(1 - K_a). \quad (23)$$

In addition to the tensile stress caused by the matrix suction, the bending moment of the overhang contributes to the total stress at the top dune surface. It is assumed that the soil is homogeneous and behaves in a linear-elastic manner, so that the dune is in tension at the top of the overhang and in compression at the bottom. Based on simple beam theory, the maximum tension due to bending at the top surface is,

$$\sigma_{bs} = -(M_b A)/(2I_o) \quad (24)$$

where $M_b$ is the per unit-length bending moment of the overhang, and $I_o$ the moment of inertia of the lengthwise cross-section (defined by $A$ times the unit length; $I_o = A^3/12$). The bending moment ($M_b$) of the overhang is (per unit length) $M_b = \gamma A_c X_c$, where $A_c$ is the cross-section area of the overhang, and $X_c$ the centroid of the overhang. With the assumption of a triangular notch, the area of the cross-section is $A_c = b_1(D_s + 1/2(A - D_s))$, and

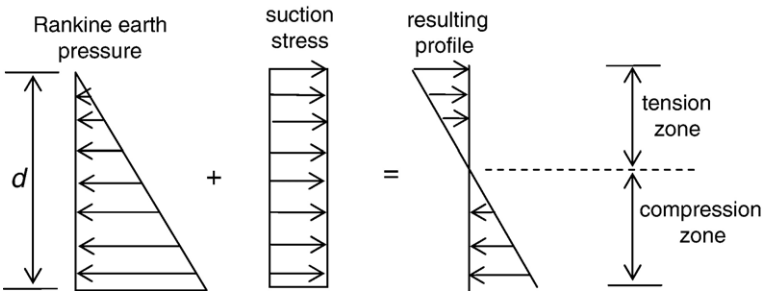


Fig. 5. Conceptual diagram of active earth pressure components of unsaturated non-cohesive soil (adapted from Lu and Likos, 2004).

the horizontal center of gravity with respect to an origin at the maximum notch depth is:

$$X_c = (b_1^2(2D_s + A))/6A_c. \quad (25)$$

## 3. Experimental design and procedure

The experiment was conducted in a 27 m section of a tank, equipped with a piston-type wave paddle, at the Engineering Research and Development Center, U.S. Army Corps of Engineers in Vicksburg, Mississippi. The tank measured 0.91 m in width, and 0.91 m at maximum depth. The set-up of the experiment is shown in Fig. 6. Uniform sand with a median grain size diameter ($D_{50}$) of 0.13 mm, a fall speed of 1.4 cm/s, and an internal (uncompacted) friction angle of 33° was used in the experiment. Specific soil density was back-calculated from the fall speed parameter reported in Hughes and Fowler (1990) and an estimated kinematic viscosity at $T$=15 °C ($\nu$=1.12E−6 m$^2$/s) yielding $\rho_s$=2690 kg/m$^3$. The beach profile beneath the still water line was graded to represent an equilibrium profile (Dean, 1977). The beach slope from just below the still water line to the dune was 1:15. An idealized shape, in the form of a vertical face (with a height of $D_o \approx 0.21$ cm), was used to represent a dune undergoing erosion (e.g., Edelman, 1968). Foreshores and dunes were constructed with wetted sand, and placed and compacted with hand tools.

For the case of scaling the experiment to a prototype dune condition, the design of the experiment was dependent on two criteria. First, the experimental set-up had to be configured so that solitons or other confused wave forms were not generated.

This was done by ensuring a depth to wavelength ratio greater than 0.09 as suggested by Galvin (1972). Secondly, the scaling criteria presented by Hughes and Chiu (1981) and Hughes and Fowler (1990) had to be met. The scaling criteria was specifically developed for physical modeling of coastal dune erosion in movable-bed models based on inertial forces, represented by turbulent shear stress, and gravity in the direction of the principal flow. Two criteria are simultaneously satisfied. The first is the Froude number representing the inertia to gravity forces of the hydrodynamics. The second is the fall speed parameter describing the morphological response to the hydrodynamics. For an undistorted scaling model, the resulting relationship is $N_w = N_t = \sqrt{N_l}$ where $N$ represents the prototype-to-model ratio of the subscribed parameter, $w$ is the fall speed parameter, $t$ is time, and $l$ is length. With a length scale factor of 10:1 (time-scale factor of 3.2:1), the corresponding prototype is a small dune on the order of 2 m in height with a sand size of $D_{50} \approx 0.41$ mm.

Parameters and wave conditions employed in the experiments are listed in Table 1a and b. Two wave conditions were employed: single solitary waves (Table 1a) and wave trains (Table 1b). Offshore wave heights, $H_o$, ranged from 6 to 10 cm for the solitary wave experiments (0.6 m to 1 m prototype). The wave trains were generated using two closely spaced harmonics of equal amplitude, resulting in wave trains with increasing and subsequently decreasing wave heights. The wave trains consisted of ten waves ranging in offshore wave heights from about 1.5 cm–2.5 cm to a maximum of 10 cm, 15 cm, or 20 cm, (1 m to 2 m prototype) depending on the test case. The wave period was 2.2 s for all wave trains (7 s prototype). Two experimental phases (A and B) were conducted for each set of wave conditions whereby the water level was raised enabling higher bores to impact the dunes. All the solitary waves broke as plunging breakers (misprint in Erikson et al., 2003) while the waves of the wave trains broke as either spilling or plunging waves before propagating upslope and hitting the dune face.

Incident bore heights ($h_{inc}$) were measured with the most landward swash gauge located 21 cm and 19 cm from the dune face for the solitary and wave train experiments, respectively. Measured average values are listed in the last columns of Table 1a and b. Video and still

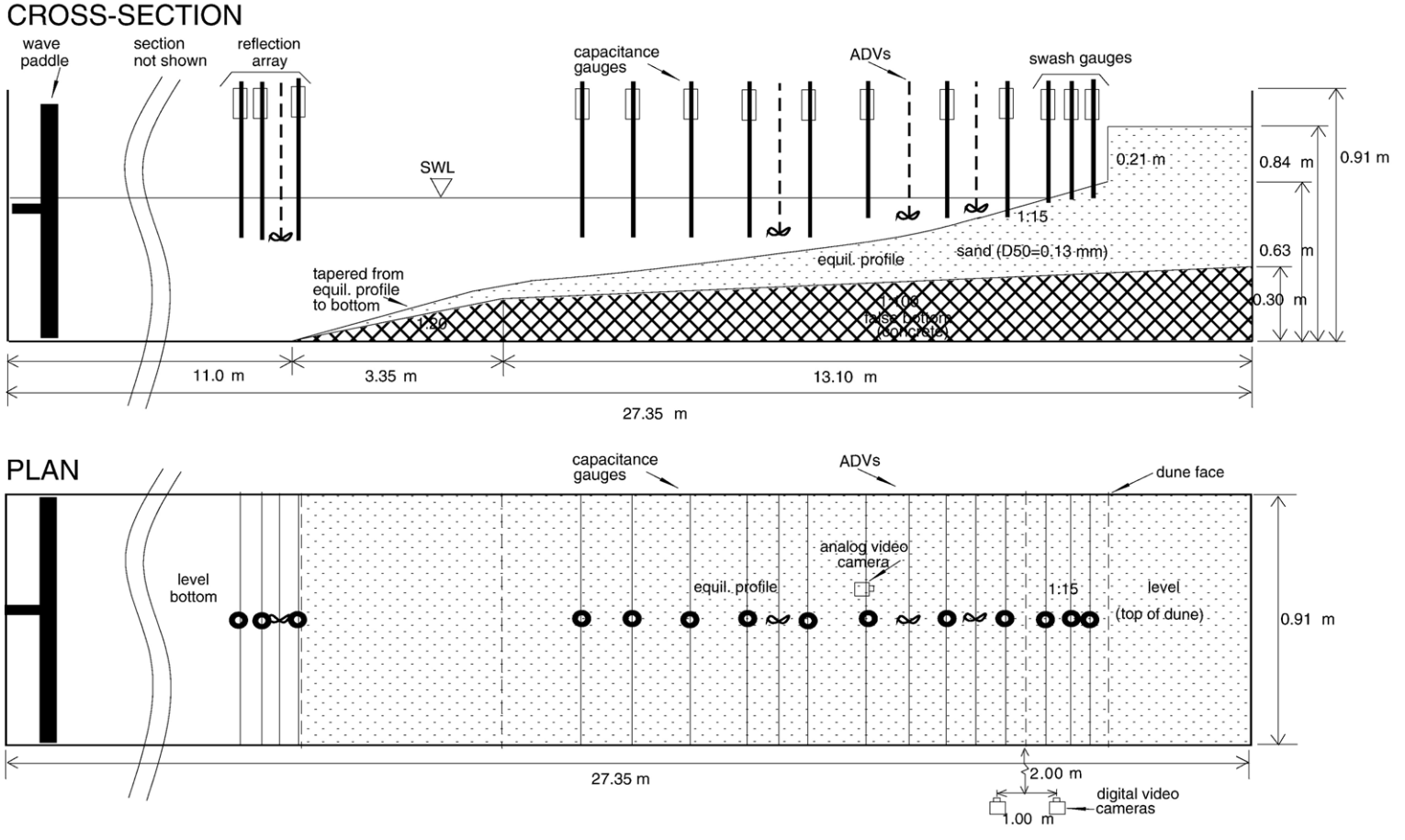


Fig. 6. Laboratory set-up. A cross-section of the tank is shown in the upper plot and a plan view is shown in the lower plot.

camera images were used to measure profile changes. The cameras were positioned about 2 m from the target so that nominal pixel resolution was better than 2 mm with a horizontal field of view less than 1.5 m for each camera. A grid of control points was marked on the outside of the glass tank wall (target plane) with an origin defined at the still water shoreline to allow post-processing rectification.

Dune and sediment properties were obtained with standardized soil tests. A cylindrical corer with an 8 cm diameter and height of 11 cm was constructed from metal sheeting to collect *in situ* samples of the dune following completion of nearly each experimental case. Samples were collected from the approximate middle of the remaining dune in the vertical and horizontal directions.

Mass failure was observed to usually occur at the center of the dune or the far facing glass wall. In most cases the dune adhered to the sidewall on the camera side. This was probably due to the lighting which was required for the cameras, but heated the glass wall and enabled the wet sand to form a strong bond. Notch evolution was quite even across the tank however, and did not seem to be affected by the sidewalls. Initially, adherence of sediments to the sidewall at mass failure was viewed as a drawback, however the occurrence works to the advantage of data collection in that it was, thus, possible to obtain the depth of the notch that formed at failure.

## 4. Experimental results

Experimental dunes were subjected to impacting waves until they failed by mass wasting. The number of bores or wave packets required for mass failure is listed in Table 2a and b along with the measured height of the overhang prior to or at mass failure, $D_s$, measured lengths from the top surface to the maximum notch depth, $A$, maximum notch depth, $b_{1cr}$, and total recession distance, $b_2$. As was done in Table 1a and b, experimental cases are listed in order of increasing offshore wave heights for each test phase. With the exception of A14 or A15, the number of bores required for collapse decreases with increasing offshore wave height, as would be expected if the dune properties were similar. The recession distance, $b_2$, is equal to the critical notch depth, $b_{1cr}$, for cases B5 and B3; these cases are hypothesized to have recessed by shear-type mass failure (Fig. 6a).

Table 1a
Experimental design and wave conditions of solitary wave experiments

| Case | Foreshore length (cm) | Water level (cm) | $H_o$ (cm) | $D_o$ (cm) | $\overline{h}_{inc}$ (cm) |
|---|---|---|---|---|---|
| A13 | 150 | 53 | 8 | 20.5 | 3.0 |
| A14 | | | 9 | 21.2 | 3.8 |
| A15 | | | 10 | 20.8 | 3.5 |
| B1 | 100 | 56 | 6 | 22.9 | 3.0 |
| B5 | | | 7 | 21.4 | 3.9 |
| B2 | | | 8 | 22.8 | 4.3 |
| B4 | | | 9 | 22.0 | 4.6 |
| B3 | | | 10 | 21.0 | 5.2 |

Table 1b
Experimental design and wave conditions of wave group experiments

| Case | Foreshore length (cm) | Water level (cm) | $H_o^a$ (cm) | $D_o$ (cm) | $\overline{h}_{inc}$ (cm) |
|---|---|---|---|---|---|
| A19 | 40 | 56 | 9 | 20.7 | 2.5 |
| A17 | | | 14 | 20.8 | 2.8 |
| A18 | | | 18 | 22.7 | 4.1 |
| B12 | 10 | 58 | 9 | 20.8 | 3.6 |
| B15 | | | 14 | 22.4 | 4.4 |
| B14 | | | 18 | 22.3 | 4.5 |

[a] Of the highest wave in the group.

Calculated geotechnical parameters obtained from soil cores are also listed in Table 2a and b. Water contents (by mass, $w$) ranged from 14% to 23% and should thus provide strengthening in the form of matrix suction. The total weight of core samples was unfortunately not obtained for the experimental cases where dunes were subjected to wave trains and therefore, the unit weight at natural moisture content, $\gamma$, porosity, $p$, degree of saturation, $S$, and related matrix suction are not available for these experiments. These values are listed for the solitary wave cases in the last four columns of Table 2a. Dune porosities (volume of voids over the total sample volume) were quite similar in the range of 0.38 to 0.41 suggesting that the dunes were slightly to moderately compacted. Saturation levels, listed in the next to last column, were quite high ($57\% < S < 89\%$) so that the effects of matrix suction could be ascertained. Although not verified, the relatively high levels possibly represent storm conditions where elevated groundwater levels, intense rain, and wave splash cause increased water contents and saturation levels of moderately compacted or consolidated sand formations.

In this study, the matrix suction was estimated with the method described by Öberg (1997) whereby the water retention curve (a plot of matrix suction vs. saturation levels) of a reference soil from Andersson and Wiklert (1972) was employed. Approximate matrix suction values, as read from the said curve, are listed in the last column of Table 2a. The matrix suction varies

Table 2a
Geometric and geotechnical parameters at failure for solitary wave tests

| Case | Bore # at collapse | $D_s$ (cm) | $A$ (cm) | $b_{1cr}$ (cm) | $b_2$ (cm) | $w$ (%) | $\gamma$ (g/cm$^3$) | $p$ | $S$ (%) | $(u_a-u_w)$ (kPa) |
|---|---|---|---|---|---|---|---|---|---|---|
| A13 | 38 | 14.7 | 15.6 | 5.1 | 8.8 | 15 | 1.85 | 0.39 | 64 | 2.57 |
| A14 | 23 | 14.7 | 16.0 | 4.9 | 9.9 | 23 | 1.92 | 0.41 | 89 | 2.07 |
| A15 | 26 | 13.2 | 15.8 | 5.5 | 7.8 | 15 | 1.84 | 0.39 | 62 | 2.58 |
| B1 | 25 | 14.3 | 18.4 | 3.9 | 8.0 | 19 | 1.80 | 0.43 | 70 | 2.35 |
| B5 | 18 | 11.4 | 16.5 | 5.4 | 5.4 | 20 | 1.96 | 0.38 | 88 | 2.19 |
| B2 | 15 | 14.3 | 17.6 | 5.2 | 8.0 | 14 | 1.82 | 0.39 | 57 | 2.67 |
| B4 | 13 | 8.8 | 16.0 | 5.1 | 8.9 | 20 | 1.87 | 0.41 | 78 | 2.27 |
| B3 | 10 | 9.1 | 17.2 | 5.0 | 5.0 | 16 | 1.79 | 0.41 | 60 | 2.57 |

only slightly (2.07 kPa to 2.67 kPa) as is typical of clean sands within the given saturation range.

## 5. Model results

Analytical models describing dune recession by erosion of the dune foot (notching) and subsequent mass failure, were developed in Section 2. In this section, the notching model is first calibrated with experimental data. The accuracy of the mass failure model is then assessed with data where dune erosion was measured on a wave-by-wave basis.

### 5.1. Notching model

Referring back to Fig. 2, an interesting result of the experiment is that the notches are all quite similar in shape. Close inspection indicates that the lower parts of the notches are linear whereas the upper portions have mostly a concave curvature. Employing the power function in Eq. (6), the $m$-exponent was found for each measured notch shape using least-squares regression. The results are plotted against offshore wave steepness ($H_o/L_o$) in Fig. 7, where the deepwater significant wave height was employed for the wave trains, and the deep-water wave lengths were approximated with $L_o=1.56T^2$ for the wave train data, and $L_o=(4.36)/\sqrt{3H_o/4h_o}$ for the solitary wave data ($h_o$=water depth, Synolakis, 1986).

Table 2b
Geometric parameters at failure for the wave group experiments

| Case | Packet # at collapse | $D_s$ (cm) | $A$ (cm) | $b_{1cr}$ (cm) | $b_2$ (cm) | $w$ (%) |
|---|---|---|---|---|---|---|
| A19 | 13 | 16.0 | 18.1 | 2.7 | 10.0 | ND |
| A17 | 11 | 12.2 | 17.2 | 3.4 | 10.9 | 18 |
| A18 | 6 | 15.6 | 20.5 | 3.3 | 8.4 | 21 |
| B12 | 6 | 14.7 | 18.1 | 4.8 | 9.0 | 22 |
| B15 | 3 | 15.0 | 19.8 | 5.3 | 8.0 | 18 |
| B14 | 3 | 13.0 | 18.5 | 6.0 | 8.2 | 19 |

ND: core sample not collected.

The coefficient of determination was 0.72 or better for each individual notch. The overall mean value of the $m$-exponent ($\bar{m}$) for the cases with solitary waves was 1.02 (standard deviation ($\sigma^2$)=0.25), whereas the overall mean for the dunes subjected to wave trains was 1.55 ($\sigma^2$=0.21). The notch shapes for the solitary wave cases thus closely resemble triangles whereas the shape seems to be better represented with a power-type formulation for the cases with wave trains. The difference may be due to the type of offshore waves although once the waves impacted the dune face, they were all fully broken bores. One parameter that appears to affect the notch shape is the wave steepness as can be seen in Fig. 7 where the $m$-exponent increases with increasing offshore wave steepness, particularly for the dunes subjected to wave trains.

#### 5.1.1. Inferred notch heights

There are three unknowns that need to be determined before Eqs. (10) and (11) can be used in a predictive mode to determine the notch depth, $b_1$: the empirical coefficient, $C_a$, the runup height, $R$, and the transport coefficient, $K_d$. The coefficient $C_a$ was introduced to account for the area of physical contact between the dune face and incident as well as reflecting bores. Following initial contact between the leading edge of the swash with the dune face, the bore front spouts upward in a jet-like manner while the additional volume of water offered by the remaining incident bore continues to pile up against the dune face increasing the area of contact until the bore reverses direction. With the aid of still images obtained from video, incident bore heights immediately before impact were obtained and compared to measured notch heights. The results for the solitary waves are shown in Fig. 8 where it is apparent that the notch heights are about 40% greater than incident bores in front of the dune face ($C_a$=1.37; $R^2$=0.98). Data from the wave trains were omitted in Fig. 8 because of the difficulty in measuring a single incident bore height in front of the dune while there are several bores present in the swash zone and interacting with one another.

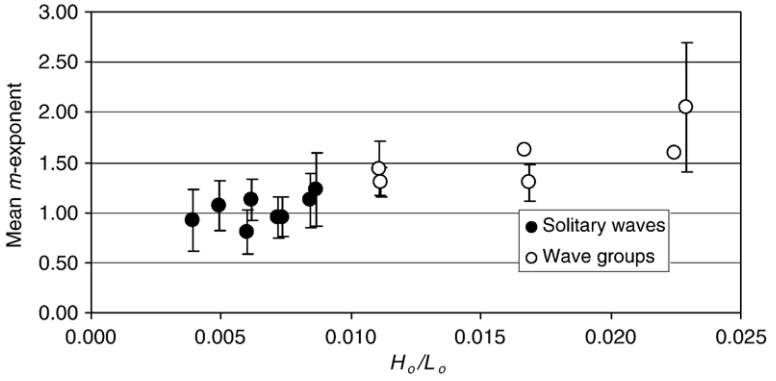


Fig. 7. Mean values of the *m*-exponents describing the shape of the upper part of the notches plotted against the offshore wave steepness. Standard deviations are shown with error bars.

The runup heights were predicted with the 'ballistics model' described by Erikson et al. (2005), including the effects of swash interaction for the wave trains. The runup model requires initial velocity at the shoreline, $u_s$, which was calculated with Eq. (3) at the SWS but with $h_{inc}$ replaced with measured wave heights at the SWS. Inputs to the model were wave heights and arrival times at the SWS. For the solitary wave data, there were only single waves and thus only one wave height was required. The coefficient $C_u$ in Eq. (3) was set to 1.83 for the wave trains (e.g., Cross, 1967) but increased to the theoretical maximum of $C_u$=2.0 for the solitary waves. Increasing $C_u$ from 1.83 to 2.00 for the solitary waves increased the runup height by about 18% and was necessary to better represent the inferred runup heights of the solitary waves. Although not clear and in need of further consideration, it is speculated that the greater coefficient reflects the lower resistance subjected on the solitary waves as compared to the oscillatory waves when they break and transition from propagating waves to translating bores.

Inferred notch heights with $C_a$=1.37, are compared to measured notch heights as shown in Fig. 9. The coefficient of determination is 0.93 with a slope of 0.92, excluding case A19 for which the calculated runup did not reach the dune. Only notch heights following impact of the first bore or wave packet were used as it could not be assumed that the top of the notch from subsequent bores resulted from the most recent bore as opposed to previous ones.

### 5.1.2. Transport coefficient

In order to describe the evolution of the notch depth on a wave-by-wave basis, Eqs. (10) and (11) were modified to yield,

$$b_{1n} = K_d 8n[(a_n/(1-p))(\rho/\rho_s)] \tag{26}$$

where $C_a$ $(R-z_{in})$ was replaced with measured values, $a_n$, and $n$ was introduced to represent the bore number. Measured notch depths, $b_1$, were then plotted against the right-hand-side of Eq. (26) (excluding $K_d$) and $K_d$-

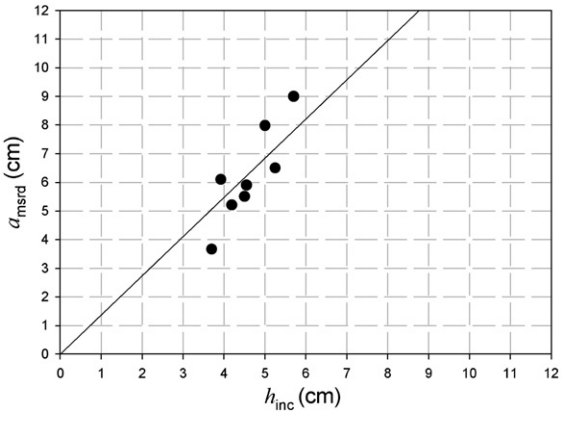


Fig. 8. Measured notch heights plotted against measured incident bore heights in front of the dune face for the solitary wave experiments.

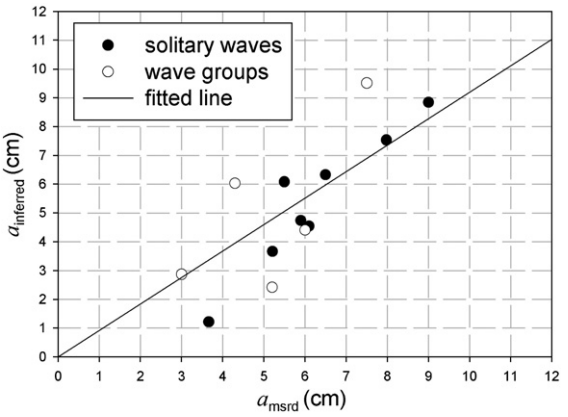


Fig. 9. Inferred versus measured notch heights, *a*.

values were determined from the slopes of least-square regression lines forced through the origin (Fig. 10). Because Eq. (26) is a function of $p$ which was not determined for the wave train data, results from the solitary wave data only have been analyzed. Measured notch areas following bore 20 were discarded for case A15 (see below). Fig. 11 plots the approximate eroded areas (volume per unit width, that is, $1/2ab_1$) against the total number of impacting bores. At bore 22, the eroded area of case A15 decreases as a result of slumped material from the notch roof and thus is not related to erosion caused by the impact of bores. Similarly, only the first 12 (out of a total of 38) bores were utilized in the analysis for case A13, where beyond that point the notch area remained fairly constant (lower line in Fig. 11) and appeared to close up as a result of accumulated sediments originating from seaward of the dune. This was also evident for the other cases with relatively low offshore wave heights, A14, B1 and B5, but not to such a significant degree (Fig. 2).

The inferred $K_d$-values and associated coefficients of determination are listed in Table 3. The coefficients of determination are quite good for all cases except B1 ($R^2=0.67$). Inspection of Fig. 10 shows that at the beginning of bore impact for case B1, the notch depth increased quite quickly and then slowed down as $b_1$ approached 2.5 cm. One possible explanation may be that the dune properties were inhomogeneous such that compaction and water content were not the same at the front of the dune compared to further back.

The transport coefficient ($K_d$) obtained with the solitary wave data ranges from 4.24E−3 to 10.4E−3 (Table 3). The variation is likely due to dependence on some geotechnical and other physical parameters not already included in the analytical model. The transport coefficient describes the rate at which notching occurs,

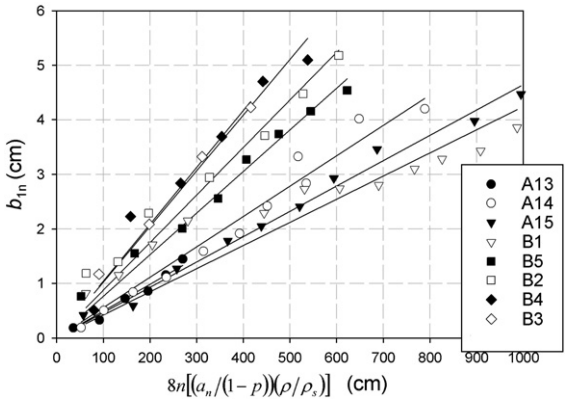


Fig. 10. Notch depth plotted against the right-hand-side of Eq. (26) for the solitary wave data. Resulting slopes are $K_d$-values.

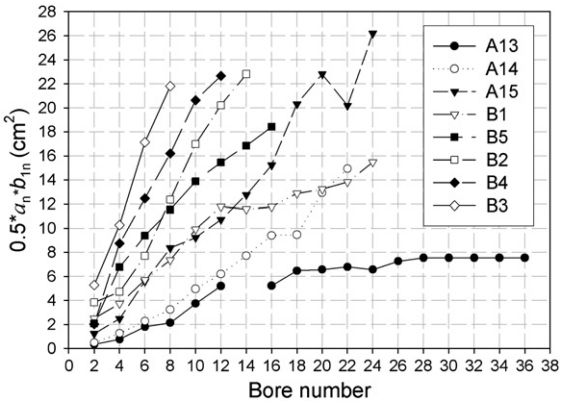


Fig. 11. Notch erosion rates.

and might be considered to be related to the ratio between the forcing at the dune and dune properties that hinder erosion, as suggested by Sunamura (1983).

Overton et al. (1994) measured dune erosion on a per-wave basis in a small wave tank with two different sediment grain sizes and compaction levels. They concluded that although dune density was statistically significant with respect to the force–erosion relationship, sediment grain size was even more important, particularly for the finer grain sands. Larson et al. (2004) found that their transport coefficient (from a slightly different version of the force–erosion relationship) was related to the ratio between the offshore wave height and sediment grain size. The dependence on sediment grain size may be related to the strengthening that matrix suction is capable of providing. Although only one grain size was used for the experiments in this study, indirect measurements of matrix suction were obtained by the method described in Section 4.

In keeping with the idea that $K_d$ is related to the ratio between the forcing at the dune and dune properties that hinder erosion, representative swash forces were multiplied by representative compaction levels and divided by the shear strength and median grain size. By combining Eqs. (3) and (4), the swash force for a single bore may be expressed as:

$$F_o = C_u^2 \rho g h_{inc}^2 \tag{27}$$

In Fig. 12, the $K_d$ coefficients obtained from Eq. (26) are plotted against the swash force (using mean

Table 3
Derived $K_d$-values and coefficients of determination

| | A13 | A14 | A15 | B1 | B5 | B2 | B4 | B3 |
|---|---|---|---|---|---|---|---|---|
| $K_d$ (*E−3) | 4.92 | 5.57 | 4.65 | 4.24 | 7.64 | 8.74 | 10.2 | 10.4 |
| $R^2$ | 0.96 | 0.97 | 0.99 | 0.67 | 0.99 | 0.94 | 0.95 | 0.99 |

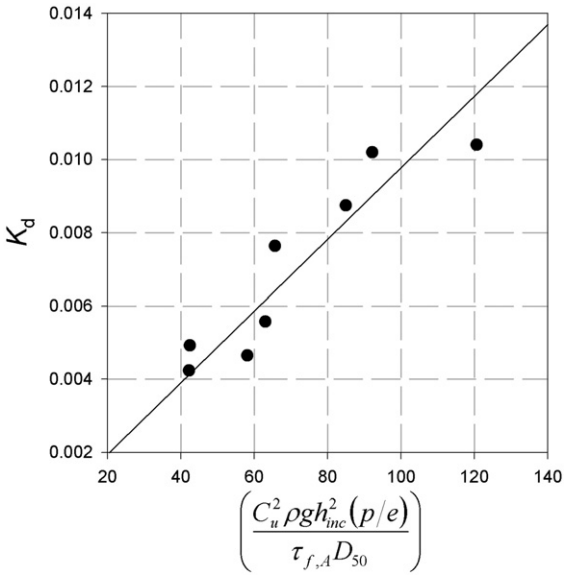


Fig. 12. Derived $K_d$-coefficients plotted against hydrodynamic forcing and geotechnical parameters.

measured incident wave heights in front of the dunes (Table 1a and b)) multiplied by the porosity over the void ratio ($p/e$), and divided by the shear strength and median grain size. The ratio $p/e$ is equivalent to the volume of solids divided by the total volume of a given sample, and is considered to represent the compaction level. The shear strength was calculated at depth $A$ so that from Eq. (15) $\tau_{f,A}=\gamma A \tan\phi' + S(u_a - u_w)\tan\phi'$ where $\tau_{f,A}$ is the soil strength provided by both the weight of overlying material and soil suction. A least-squares regression with $C_u=1.83$ suggests a linear relationship passing through the origin ($R^2=0.84$):

$$K_d = 0.97 \cdot 10^{-4}\left(\frac{C_u^2 \rho g\, \overline{h}_{inc}^{\,2}(p/e)}{\tau_{f,A} D_{50}}\right). \quad (28)$$

The sediment grain size, $D_{50}$, was introduced in Eq. (28) to ensure a dimensionless $K_d$. The resulting fitted linear line has a positive slope suggesting that if $D_{50}$ is allowed to increase, $K_d$ will decrease. However, Overton et al. (1994) found that their transport coefficient decreased with decreasing grain size. Hence, Eq. (28) is probably only valid for a given grain size (i.e., $D_{50}$=constant), although this was not tested with the data obtained for this study as only one grain size was employed in the experiments. In addition, care should be taken in using Eq. (28) as it stems from a limited data set and is only valid for the approximate range $20<(C_u^2\rho g h_{inc}^{-2}(p/e))/(\tau_{f,A}D_{50})<140$.

### 5.2. Mass failure model

Equations presented in Section 2.2 were applied to the experimental data to predict the dune recession distance, $b_2$. Analysis of the data from the wave train experiments is not possible as the saturation levels ($S$) and void ratios ($e$) are unknown. Although a tensile crack formed landward of the overhang for all experiments, mass wasting of the overhang only (Figs. 1(a–b) and 4a) occurred, leaving the remaining dune intact for both cases B5 and B3. The shear-type failures occurred when $b_{1cr}$ (=$b_{2shear}$) was 5.4 cm and 5.0 cm, for cases B5 and B3, respectively. Predicted values using Eq. (14) in conjunction with calculated shear strengths (Eq. (15)) are off by no more than 10% with 5.1 cm and 5.9 cm, for B3 and B5 respectively.

Recession of the remaining experimental dunes occurred by beam-type failures. The landward location of the tensile crack ($b_{2beam}$) was estimated by determining the length of a tensile crack that might be expected to develop given the tensile strength of the soil and stresses generated by lateral earth pressures and bending moments. Calculated tensile strengths were computed with Eq. (18), range from 0.74 to 2.05 kPa, and are listed in the second column of Table 4. Stresses at the surface due to lateral earth pressures, $\sigma_{LEPs}$, and bending moments ($\sigma_b$) are listed in the third and fourth columns, while the final column lists the (combined) total stress at the surface, $\sigma_{ss}$.

It is interesting to note that for the majority of cases (A13, A15, B1, B2, B3, and B4) $\sigma_{LEPs}>\sigma_t$ suggesting that notching was not necessary in order for tensile cracking to occur. Although tensile cracking may have occurred due to the lateral earth pressure alone, the small difference between $\sigma_t$ and $\sigma_{LEPs}$ results in very small tensile crack depths ($Z_c$, Eq. (17)) so that by geometry (Eq. (16)), $b_{2beam}$ becomes about twice as large as measured. Alternatively, one might consider that the lateral earth pressure alone is responsible for the tensile

Table 4
Comparison of tensile strengths and stresses (kPa) computed for the beam-failure model

| Case | $\sigma_t$ | $\sigma_{LEPs}$ | $\sigma_b$ | $\sigma_{ss}$ |
|---|---|---|---|---|
| A13 | 1.09 | 1.15 | 0.85 | 2.00 |
| A14 | 1.58 | 1.31 | 0.86 | 2.17 |
| A15 | 1.02 | 1.13 | 0.74 | 1.87 |
| B1 | 0.90 | 1.19 | 0.38 | 1.57 |
| B5 | 2.05 | 1.36 | 0.00 | 1.36 |
| B2 | 0.93 | 1.08 | 0.69 | 1.77 |
| B4 | 1.20 | 1.24 | 0.67 | 1.91 |
| B3 | 0.74 | 1.08 | 0.00 | 1.08 |

crack reaching down to an internal failure plane starting from the initial dune foot prior to any notching. However, this too over-predicts the recession distance but only by about 2 cm. It is speculated that for these cases where $\sigma_{LEPs} > \sigma_t$, failure did not occur because the shear stress on the internal failure plane did not exceed the shear strength. This was tested by computing the shear stress on the inclined failure plane,

$$F_3 = W_b \sin(45° + \phi'/2) \quad (29)$$

where $W_b$ is the weight of the failure block. The opposing force was estimated with,

$$F_2 = \tau_{cr} L \quad (30)$$

where $L$ is the length along the internal failure plane that remains attached after a tensile crack has formed ($=b_3/\cos\alpha$). The calculated forces are compared in Table 5a for the cases where $\sigma_{LEPs} > \sigma_t$ and for the described scenarios. The last three columns compare the shear stress and strength with $b_3$ predicted by accounting for stresses due to both the lateral earth pressures and bending moment. In the first two scenarios, where the bending moment is not accounted for, the total shear strength ($F_2$) exceeds the gliding force ($F_3$) generated by a block defined by the predicted geometry, thus supporting the notion that failure did not occur due to lateral earth pressures alone. In all cases where the bending moment is accounted for, $F_3 > F_2$ and thus predicts that failure would occur. With the exception of case B3, this is further supported by the much better comparison between measured and calculated $b_3$ values as compared to the other two scenarios. The beam-type model predicts that the dune of case B3 should fail by tensile cracking and subsequent shear failure along the internal failure plane with a resulting $b_3 = 5.8$ cm ($b_2 = 10.8$ cm). Development of a tensile crack was observed at about 8 cm although failure at this point did not occur. Instead, the overhang alone failed with the remaining material landward of the maximum notch depth intact. The discrepancy for this is uncertain but might simply be because the shear failure occurred prior to the beam-type failure.

Table 5b
Overturning and resisting moments with and without bending stresses

| Case | $M_o$ (N) | Resisting moment, $M_r$ (N) | |
|---|---|---|---|
| | | $\sigma_{LEPs}$ only and with $\alpha$ from max notch depth | $\sigma_{ss}$ and with $\alpha$ at notch depth |
| A13 | 3.5 | 11.0 | 1.3 |
| A15 | 3.8 | 10.7 | 1.1 |
| B1 | 2.2 | 11.7 | 3.4 |
| B2 | 3.5 | 13.7 | 2.7 |
| B4 | 2.9 | 13.6 | 2.1 |
| B3 | 2.8 | 7.6 | 4.1 |

Only cases for which $\sigma_{LEPs} > \sigma_t$ are listed.

Besides the possibility of shear failure along the internal failure plane following tensile cracking, there is a potential for failure by overturning as depicted in Fig. 1e. This was assessed by calculating the moments about the pivot point assumed to coincide with the maximum notch depth. The overturning moment was thus defined by the moment of the overhang, while the resisting moment was calculated by multiplying the weight of the failing block material landward of the notch depth by its horizontal center of gravity (neglecting any tensile strength offered by the lower part of the pending failure block). The results are shown in Table 5b for the scenario where only the stress due to the lateral earth pressure is accounted for and second, for the scenario where both lateral earth pressures and bending moments contribute. For the scenario where only the lateral earth pressure is accounted for, the resisting moment exceeds the overturning moment supporting the notion that the block did not fail with the given geometry. For the case where the bending moment is included in the tensile stress analysis, the overturning moment exceeds

Table 5a
Sliding and resisting forces for scenarios with and without bending stresses

| Case | Msrd $b_3$ (cm) | $\sigma_{LEPs}$ only at $t=0$ and with $\alpha$ from initial dune foot | | | $\sigma_{LEPs}$ only and with $\alpha$ from max notch depth | | | $\sigma_{ss}$ and with $\alpha$ at notch depth | | |
|---|---|---|---|---|---|---|---|---|---|---|
| | | Predicted $b_3$ (cm) | $F_3$ (N/m) | $F_2$ (N/m) | Predicted $b_3$ (cm) | $F_3$ (N/m) | $F_2$ (N/m) | Predicted $b_3$ (cm) | $F_3$ (N/m) | $F_2$ (N/m) |
| A13 | 3.7 | 5.4 | 185 | 299 | 8.5 | 238 | 272 | 3.3 | 189 | 139 |
| A15 | 2.3 | 4.7 | 188 | 289 | 8.6 | 252 | 277 | 2.9 | 188 | 129 |
| B1 | 4.1 | 5.7 | 216 | 295 | 10.0 | 292 | 332 | 4.9 | 211 | 187 |
| B2 | 2.8 | 5.7 | 224 | 306 | 9.6 | 283 | 299 | 4.4 | 223 | 171 |
| B4 | 3.8 | 6.4 | 216 | 353 | 8.7 | 228 | 289 | 4.1 | 190 | 166 |
| B3 | 0.0 | 2.9 | 171 | 225 | 9.3 | 282 | 295 | 5.8 | 216 | 198 |

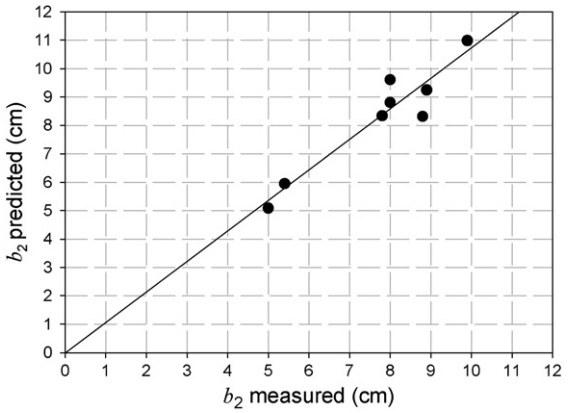


Fig. 13. Measured versus predicted recession distances.

the resisting moment in all cases except one, case B1. Hence it appears that (1) the dune of case B1 failed by tensile cracking and shear failure along the internal failure plane, and (2) the dunes of cases A13, A15, B2, and B4 failed by tensile cracking and shear along the internal failure plane or overturning or a combination of both. For case A14, for which $\sigma_{ss} > \sigma_t$ but $\sigma_{LEP} < \sigma_t$, and therefore not listed in Table 5a and b, the gliding force ($F_3 = 228$ N/m) exceeds the shear strength ($F_2 = 24$ N/m) along the predicted internal failure plane and the overturning moment ($M_o = 368$ Nm/m) exceeds the resisting moment ($M_r = 345$ Nm/m) so that failure by tensile cracking and one or a combination of the aforementioned mechanisms is expected.

Results for recession distances due to mass wasting are shown in Fig. 13. The predicted $b_3$ values obtained with the beam-type failure model were added to the notch depths ($b_{1cr}$) to give the full recession distances, $b_2$, and compared to measured values. Results for the shear-type failures are also given, and together they show a good fit with $R^2 = 0.90$ and a slope equal to 1.07 (slope of 1 denotes perfect fit). Beam-type failure occurred in six of the eight cases. Shear failure occurred for cases B5 and B3 and are the smaller recession distances toward the lower end of the plot. Laboratory observations largely confer with this finding in that for the shear-failures, the top of the failure block remained facing upward as it slid bodily downward, while the mass failures of the beam-type failures either toppled over so that the top of the failure block faced toward the paddle or slid downward so the top remained facing upward.

## 6. Discussion and conclusions

A small wave tank study was conducted to gain further understanding and to quantify the mechanisms involved in dune recession. Idealized small-scale experimental dunes were subjected to two sets of wave conditions at separate occasions: fully broken single solitary waves and wave trains with increasing and subsequently decreasing wave heights. Solitary waves were employed to investigate the effects of dune erosion on a wave-by-wave basis. Recession occurred as a two-step process whereby the impact of waves formed a notch at the dune foot resulting in a mass instability that caused mass failure. Two modes of mass failure were observed: shear- and beam-type. In shear-type failures, the weight of the overhang exceeds the shear strength of the sediments so that the failure block slides downward or topples over. Beam-type failure, whereby a tensile crack forms some distance landward of the maximum notch depth, was observed in the majority of the experiments.

Three models were developed to describe the dune recession: first, a notching model predicting the amount eroded at the dune foot, second, a model predicting mass failure by shearing, and lastly mass-failure whereby the soil tensile strength is exceeded. The upper portion of the notches was shown to be strongly linear for cases where the dunes were subjected to fully broken solitary waves, whereas the upper shapes were predominantly concave when impacted by wave trains of increasing and subsequently decreasing wave heights. Although non-definitive, the data suggests that concavity increases with increasing offshore wave height. Based on a generalized triangular-shaped notch, a model describing erosion at the toe of the dune was developed. A coefficient describing the erosion rate was found to be linearly related to the ratio of the forcing at the dune (incident wave height) and level of compaction normalized by the soil shear strength and median grain size diameter.

Equations describing shear- and beam-type mass wasting were developed for eroding dunes assuming triangular-shaped notches. Of the two experimental cases that resulted in a shear-type failure, the maximum error between the measured and predicted critical notch depth was less than 0.9 cm (10%). The mechanism by which beam-type failure occurs is hypothesized to occur by tensile cracking at the top surface of the dune followed by shear failure along an internal failure plane or overturning due to the weight of the overhang. It is speculated that a vertical tension crack forms some distance back from the dune face and landward of the maximum notch depth as a result of the lateral earth pressures and instability caused by the overhang (generated by erosion of the foot). When the stress exceeds the soil tensile strength, cracking begins and migrates downward until it intersects with an internal failure plane. Failure is then expected to continue if the force generated by the gliding weight of the failing slab

exceeds the shear strength of the soil along the inclined internal failure plane or if the overturning moment exceeds the resisting moment. The beam-type failure model is driven by soil tensile strength and geometric considerations. For the given data set the mean absolute error between measured and calculated recession distances due to beam-failure was 0.7 cm (9%) with a maximum of 1.6 cm (20%). In an overall sense, calculated recession distances using the two models to describe mass wasting (i.e., shear-type and beam-type failures) compare well with measured values resulting in $R^2 = 0.90$ and a slope of 1.07 with a fitted least-squares linear regression.

The models presented here provide methods to predict dune erosion at the toe and recession distances of the dune face knowing incident wave height, initial dune geometry, and a few geotechnical parameters (porosity, unit weight, and saturation level). Although the measured and inferred geotechnical parameters provide sound physical explanations for the erosion and recession mechanisms in addition to calculated values that compare well with measured quantities, there was little variation in the data. Field conditions are likely to be quite more complex than those simulated in the laboratory experiment and as such, the model should be seen as a basis for possible future investigations of more complex situations (e.g., variations in sand formations due to bedding configurations, mineral leaching and organic matter content, and variable moisture content).

## Acknowledgements

Drs. Ryuichiro Nishi at Kagoshima University and Atilla Bayram of Han-Padron Assoc. are both gratefully acknowledged for their assistance in the laboratory and for valuable discussions. Financial support for LE and HH was provided by Vinnova (Swedish Agency for Innovation Systems, contract No. 1998-0188), and by the Swedish Research Council (VR) for ML. Support for the laboratory experiment and part of the work was provided by the Coastal Inlets Research Program, Inlet Channels and Geomorphology Work Unit. Dr. Nicholas C. Kraus at the ERDC, Coastal and Hydraulics Laboratory made the laboratory experiments possible and contributed with guidance, comments, and suggestions. Comments from manuscript reviewers were very helpful and are greatly appreciated.

## References

Andersson, S., Wiklert, P., 1972. Investigation of physical properties of cultivated soils. J. Agric. Land Improve. 25 (2–3), 53–143 (Uppsala, Sweden).

Carter, R., Stone, G., 1989. Mechanisms associated with the erosion of sand dune cliffs, Magilligan, Northern Ireland. Earth Surf. Processes Landf. 14 (1), 1–10.

Carter, R., Hesp, P., Nordstrom, K., 1990. Erosional landforms in coastal dunes. In: Nordstrom, K., Psuty, N., Carter, B. (Eds.), Coastal Dunes: Form and Process. John Wiley and Sons, Inc., pp. 217–250.

Cross, R.H., 1967. Tsunami surge forces. J. Waterw. Harb. Div. ASCWE 94 (WW4), 201–231.

Dean, R.G., 1977. Equilibrium beach profiles: U.S. Atlantic and Gulf Coasts. Ocean Engineering Report, vol. 12. Department of Civil Engineering, University of Delaware, Newark.

Edelman, T., 1968. Dune erosion during storm conditions. Proc. 11th Coastal Engineering Conference, pp. 719–722.

Erikson, L., Larson, M., Hanson, H., Kraus, N.C., Nishi, R., 2003. Prediction of notching and mass failure of dunes. Proc. of Coastal Sediments '03, ASCE, CD-ROM, World Scientific Publishing Corp. and East Meets West Productions.

Erikson, L., Larson, M., Hanson, H., 2005. Prediction of swash motion and run-up including the effects of swash interaction. Coast. Eng. 52, 285–302.

Fisher, J., Overton, M., 1984. Numerical model for dune erosion due to wave uprush. Proc. 20th Coastal Engineering Conference. ASCE, pp. 1553–1558.

Fisher, J., Overton, M., Chrisholm, T., 1986. Field measurements of dune erosion. Proc. 20th Coastal Engineering Conference. ASCE, pp. 1107–1115.

Flemmer, C., 1991. On the regime boundaries of moisture in granular materials. Powder Technol. 66 (2), 191–194.

Galvin, C.J., 1972. Wave breaking shallow water. In: Meyer, R.E. (Ed.), Waves on Beaches and Resulting Sediment Transport. Academic Press.

Hughes, S.A., Chiu, T., 1981. Beach and dune erosion during severe storms. Report UFL/COEL-TR/043. Coastal and Oceanographic Engineering Department, University of Florida, Gainesville, Florida.

Hughes, S.A., Fowler, J., 1990. Midscale physical model validation for scour at coastal structures. Technical Report CERC-90-8. Coastal Engineering Research Center, Department of the Army, Waterways Experiment Station.

Kim, T.-H., Hwang, C., 2003. Modeling of tensile strength on moist granular earth material at low water content. Eng. Geol. 69, 233–244.

Larson, M., Erikson, L., Hanson, H., 2004. An analytical model to predict dune erosion due to wave impact. Coast. Eng. 51, 675–696.

Lohnes, R., Handy, R., 1968. Slope angles in friable loess. J. Geol. 76 (3), 247–258.

Lu, N., Likos, W., 2004. Unsaturated Soil Mechanics. J. Wiley Publishers, Hoboken, New Jersey. 556 pp.

Miller, R.L., 1968. Experimental determination of run-up of undular and fully developed bores. J. Geophys. Res. 73 (14), 4497–4510.

Nishi, R., Kraus, N., 1996. Mechanism and calculation of sand dune erosion by storms. Proc. 25th Coastal Engineering Conference. ASCE, pp. 3034–3047.

Öberg, A.-L., 1997. Matrix suction in silt and sand slopes: Significance and practical use in stability analysis. Ph.D. Thesis, Chalmers University of Technology, Göteborg, Sweden.

Overton, M., Fisher, J., 1988. Laboratory investigation of dune erosion. J. Waterw. Port Coast. Ocean Eng. 114 (3), 367–373.

Overton, M., Pratikto, W., Lu, J., Fisher, J., 1994. Laboratory investigation of dune erosion as a function of sand grain size and dune density. Coast. Eng. 23, 151–165.

Pierrat, P., Caram, H., 1997. Tensile strength of wet granular materials. Powder Technol. 91, 83–93.

Schubert, H., 1972. Investigation and determination of capillary pressure and suction of moist granular material (in German), Ph.D. Dissertation, Karlsruhe University, Germany.

Shen, M.C., Meyer, R., 1963. Climb of a bore on a beach: 3 run-up. J. Fluid Mech. 16, 113–125.

Sunamura, T., 1983. Processes of sea cliff and platform erosion. In: Komar, P. (Ed.), Handbook of Coastal Processes and Erosion. CRC Press, Boca Raton, pp. 233–265.

Synolakis, C., 1986. The run-up of long waves, Ph.D. Thesis, California Institute of Technology.

Terzaghi, K., 1943. Theoretical Soil Mechanics. John Wiley and Sons. 510 pp.

Terzaghi, K., Peck, R., 1948. Soil Mechanics and Engineering Practice. John Wiley and Sons, Inc. 566 pp.

Thorne, C.R., Tovey, N.K., 1981. Stability of composite river banks. Earth Surf. Processes Landf. 6, 469–484.